

RING-DIAGRAM ANALYSIS OF THE STRUCTURE OF SOLAR ACTIVE REGIONS

SARBANI BASU

Astronomy Department, Yale University, P.O. Box 208101, New Haven, CT 06520-8101; basu@astro.yale.edu

H. M. ANTIA

Tata Institute of Fundamental Research, Homi Bhabha Road, Mumbai 400005, India; antia@tifr.res.in

AND

RICHARD S. BOGART

Center for Space Science and Astrophysics, Stanford University, HEPL A202, Stanford, CA 94305-4085; rbogart@spd.aas.org

Received 2004 March 10; accepted 2004 April 12

ABSTRACT

We measure differences in structure between active and quiet regions of the Sun using the frequencies of high-degree modes determined from ring-diagram analyses. We find that both the speed of sound and the adiabatic index Γ_1 differ in active regions as compared with quiet regions. In the immediate subsurface layers, the sound speed is lower in active regions, but below a depth of about 7 Mm the opposite is true. A comparison of sound-speed inversion results with those for Γ_1 indicates that at least a part of the differences between active and quiet regions is likely to be due to the structural and thermal perturbations caused by magnetic fields in the active region.

Subject headings: Sun: activity — Sun: interior — Sun: oscillations

1. INTRODUCTION

Seismic data have been successfully used to determine the solar interior structure (e.g., Gough et al. 1996). The mean frequencies of the global modes used in these studies only give the spherically symmetric part of the structure. Departures from spherical symmetry can be studied using even-order splitting coefficients (e.g., Antia et al. 2001), but these only yield the azimuthally averaged latitudinal variations in the solar structure. To study localized variations such as those in active regions, we need to use local helioseismic techniques, e.g., ring-diagram analysis (Hill 1988) and time-distance techniques (Duvall et al. 1993). There have been some time-distance studies of the structure of sunspots (Kosovichev et al. 2000, 2001), where it was found that the sound propagation speed was lower in sunspots just below the surface and higher at greater depths.

In this work we attempt to study the differences in subsurface structure between magnetically active and quiet regions using the ring-diagram technique. Ring-diagram analyses have shown that the frequencies of modes in active regions are much higher than those in quiet regions (Hindman et al. 2000; Rajaguru et al. 2001). These frequency differences could be inverted to look for differences in structure between the active and the quiet regions. However, in ring-diagram analysis one studies regions of finite horizontal size, typically 15° (180 Mm) diameter on the solar surface. The horizontal size of the regions studied in this technique is dictated by the resolution in the resulting power spectra. Hence, the spatial resolution of these studies is not sufficient to probe the structure of an individual sunspot or a sunspot group. Nevertheless, it is possible to compare the average properties in an active area with those in a quiet region of comparable size. Such studies can give an idea of the vertical extent of sunspots and some indication of how the magnetic field varies with depth. Although ring-diagram analysis has much poorer spatial resolution than time-distance analysis, it has the advantage that the physics of ring-diagram analysis is at present better understood than that of time-distance helioseismology. Ring-diagram analysis is

based on the physics of normal modes, which are reasonably well understood, while the interpretation of time-distance analyses depends on the propagation of waves in a dispersive medium; the response functions and properties are still being worked out (e.g., Birch et al. 2001; Korzennik 2001; Gizon & Birch 2002; Jensen et al. 2003). This work should provide an independent check of the results obtained using the time-distance technique.

The rest of the paper is organized as follows. In § 2 we discuss the analysis technique and the regions studied, we give a brief description of the inversion process in § 3, and we describe and discuss our results in § 4 and state our conclusions in § 5.

2. DATA

The basic data set consists of the full-disk Dopplergrams obtained by the Michelson Doppler Imager (MDI) on board the *Solar and Heliospheric Observatory* (SOHO). Ring diagrams are three-dimensional power spectra of short-wavelength modes in a small region of the Sun. High-degree (short-wavelength) modes can be approximated as plane waves over a small area of the Sun as long as the horizontal wavelength of the modes is much smaller than the solar radius. Ring diagrams are obtained from a time series of Dopplergrams of a specific area of the Sun tracked with the mean rotation velocity. The three-dimensional Fourier transform of this time series gives the power spectra. These power spectra are referred to as ring diagrams because of the characteristic ringlike shape of regions where the power is concentrated in sections of constant temporal frequency, reflecting the near-azimuthal symmetry of the power in k -space. A detailed description of the ring-diagram technique is given by Patrón et al. (1997) and Basu et al. (1999).

For this work we have chosen to analyze a set of 12 active regions. Magnetograms of each of these regions at the times of central meridian passage are shown in Figure 1, and their characteristics are summarized in Table 1. Selection of the active regions was dictated in part by the times at which MDI was in its so-called Dynamics Program observing mode,

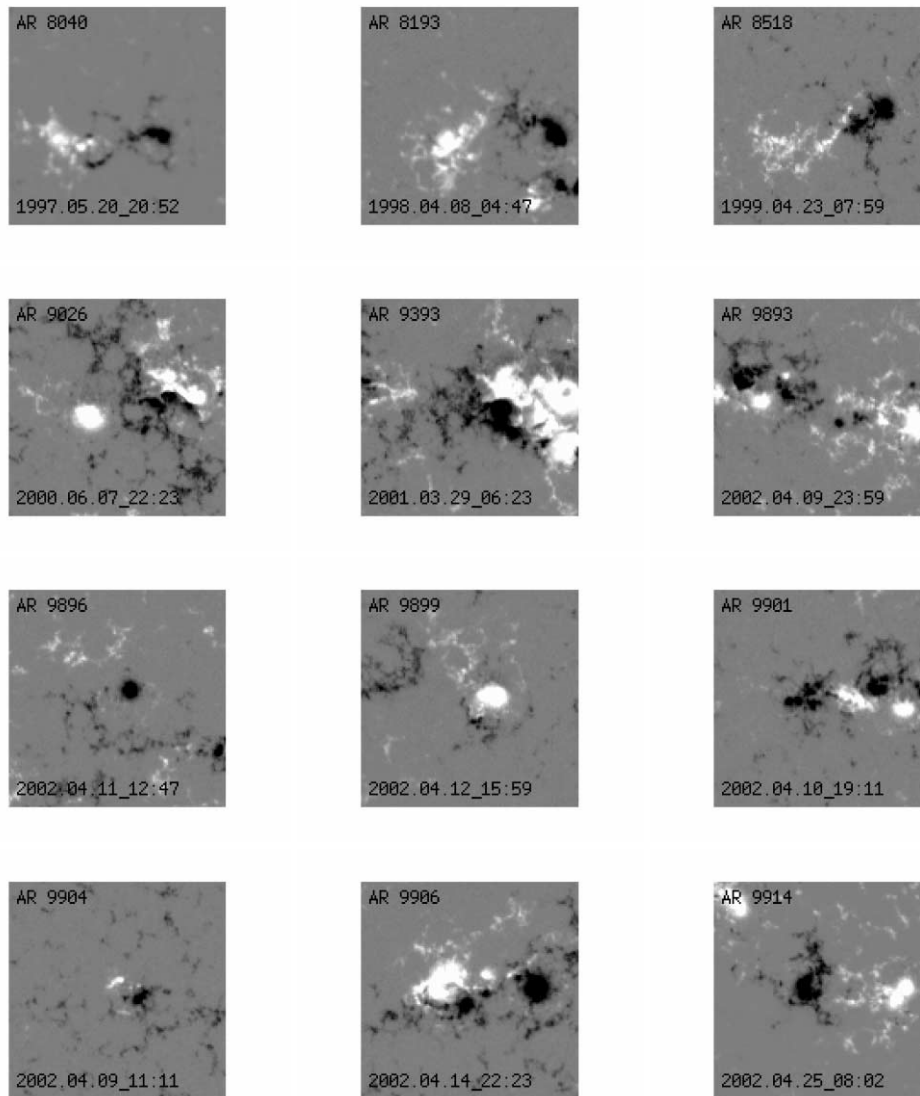


FIG. 1.—MDI line-of-sight magnetograms of each of the 12 active region areas selected for study, remapped as analyzed, at the nearest available times to those of central meridian crossing of the nominal active region location. Note that while the regions shown are square (in this mapping), the actual analysis is carried out only within the maximum inscribed circles. Thus, the area of strong positive field northeast of AR 9914, for example, which is actually part of AR 9915, would not have contributed.

for which full-disk Dopplergrams at a 1 minute cadence are available nearly continuously (at a greater than 85% duty cycle) over periods of at least the duration of the analysis interval, which in this case was at least 7 days. The regions were chosen to cover a wide range of activity levels. In order to parametrize the activity level, we defined a magnetic activity index (MAI) appropriate to the observing window and interval. The calculation of the index is described in the Appendix. We also tried to quantify the evolutionary state of the active regions involved by introducing a nondimensional growth rate parameter GR describing the rate of change of strong flux; this parameter is also described in the Appendix.

All of the active regions studied were sufficiently long-lived to be visible in magnetograms during the following Carrington rotation, and all but a few (NOAA 8040, 8193, and 9904) could be reasonably identified with spot groups receiving new numbers on the subsequent disk passage. About half had been visible during the previous rotation. Most of them were stable over the range of time they were tracked, with nondimen-

sionalized flux growth rates $|GR| < 0.3$. There were a few exceptions. NOAA 8040 and 9904, the weakest regions studied, were growing significantly, while NOAA 8193, 9026, and to a lesser extent 8518, were decaying in strength. Region 8040 was newly emergent at the start of tracking, and 9904 only emerged shortly after the central meridian passage of the tracked area. Flux growth rates were in general agreement with growth or diminution of total reported spot areas during the tracking intervals.

In order to eliminate systematic errors in the data, we invert the frequency differences between the active area and a nearby quiet area at the same latitude rather than the frequency differences between the different regions and a solar model. There are a number of different reasons for possible systematic errors. The projection of the spherical solar surface onto a flat map introduces some foreshortening that depends on the distance of the region from disk center, and this can introduce systematic errors in determining the mode characteristics. By selecting comparison regions at the same latitude and nearby

TABLE 1
COORDINATES AND PROPERTIES OF THE DIFFERENT PAIRS OF ACTIVE AND QUIET REGIONS THAT WERE ANALYZED

Region	Carrington Rotation	Latitude (deg)	Longitude ^a (deg)	MAI (G)	NOAA AR	Type ^b	Maximum Area (millionths)	Growth Rate
1.....	1922	7N	016	19.9	8040	β	150	1.18
2.....	1922	7N	341	0.2
3.....	1934	21S	082	68.4	8193	β	290	-0.77
4.....	1934	21S	067	0.6
5.....	1948	14S	105	53.2	8518	β	170	-0.41
6.....	1948	14S	075	0.9
7.....	1963	20N	071	146.6	9026	$\beta\gamma\delta$	820	-0.84
8.....	1963	20N	126	0.9
9.....	1963	20N	041	4.4
10.....	1974	19N	147	241.6	9393	$\beta\gamma\delta$	2440	0.02
11.....	1974	19N	207	1.2
12.....	1988	19N	215	81.5	9893	$\beta\gamma\delta$	490	0.14
13.....	1988	19N	255	0.7
14.....	1988	11S	195	26.8	9896	α	110	-0.24
15.....	1988	11S	205	2.0
16.....	1988	18N	180	56.3	9899	β	220	-0.26
17.....	1988	18N	240	2.2
18.....	1988	20N	204	108.5	9901	$\beta\gamma$	350	0.29
19.....	1988	20N	249	0.7
20.....	1988	16S	222	23.3	9904	β	60	0.94
21.....	1988	16S	242	2.7
22.....	1988	15S	150	125.8	9906	$\beta\gamma\delta$	850	0.28
23.....	1988	15S	120	2.8
24.....	1988	4N	013	86.9	9914	β	260	0.28
25.....	1988	4N	028	1.1

^a Central meridian longitude.

^b At central meridian passage.

Carrington longitudes and tracking both in time intervals symmetric about their central meridian passages, we assure that the foreshortening effects are nearly identical, except for small second-order effects caused by the latitudinal motion of the observer in the heliographic frame and scale changes due to radial motion of the observer. Another reason for comparing pairs of active and quiet regions at the same latitude is that MDI images are known to have a certain amount of distortion that changes with position on the disk. Again, scale changes due to this distortion will be identical for regions following the same trajectory across the disk, and to first order, regions at the same latitude and nearby longitudes will do so. Also, the analysis technique itself involves certain approximations, since the spherical solar surface layers are modeled as being plane-parallel.

Table 1 lists the active regions used in this work and their characteristics, including MAI, magnetic field configuration, etc. Also listed in the table are the comparison quiet areas for each case. In addition, we choose two pairs of quiet regions to act as control regions. These are pair Q1, which consists of regions number 13 and 17 in Table 1, and pair Q2, which consists of regions number 8 and 9 in Table 1.

To obtain the oscillation frequencies in each of these active regions and their corresponding quiet regions, we selected squares mapped in Postel's projection of size 16° in heliographic arc, with the nominal coordinates of the active regions or the comparison quiet region centered in the square. Each region was tracked for 8192 minutes centered on the time of its central meridian crossing. This follows it through about 75° of Carrington rotation. The tracked data were apodized to circular regions with an equivalent diameter of 15.8 (see the Appendix for the form of the apodization function). The power spectrum

was calculated and then fitted using the model described by Basu & Antia (1999):

$$P(k_x, k_y, \nu) = \frac{e^{B_1}}{k^3} + \frac{e^{B_2}}{k^4} + \frac{\exp [A_0 + (k - k_0)A_1 + A_2(k_x/k)^2 + A_3(k_x k_y/k^2)] S_x}{x^2 + 1}, \quad (1)$$

where

$$x = \frac{\nu - ck^p - U_x k_x - U_y k_y}{w_0 + w_1(k - k_0)}, \quad (2)$$

$$S_x = S^2 + (1 + Sx)^2, \quad (3)$$

and the 13 parameters $A_0, A_1, A_2, A_3, c, p, U_x, U_y, w_0, w_1, S, B_1,$ and B_2 are determined by fitting the spectra using a maximum likelihood approach (Anderson et al. 1990). We fit each ridge separately as explained by Basu et al. (1999). The parameter S measures the asymmetry in the peak profile. The form of asymmetry is the same as that used by Nigam & Kosovichev (1998). Of the fitted model parameters, the parameter of interest to us is the frequency, $\nu = ck^p$, of the oscillation modes as a function of their horizontal wavenumber k and radial order n . Although the oscillations in a plane-parallel geometry are only discrete in radial order, for convenience we denote the set of parameters determined by each of the fits at a selected value of k as a mode. Furthermore, the wavenumber k can be identified with the degree l of a spherical harmonic mode of global oscillations. In this study the degree l need not be an integer, as it is merely a measure of the horizontal wave number,

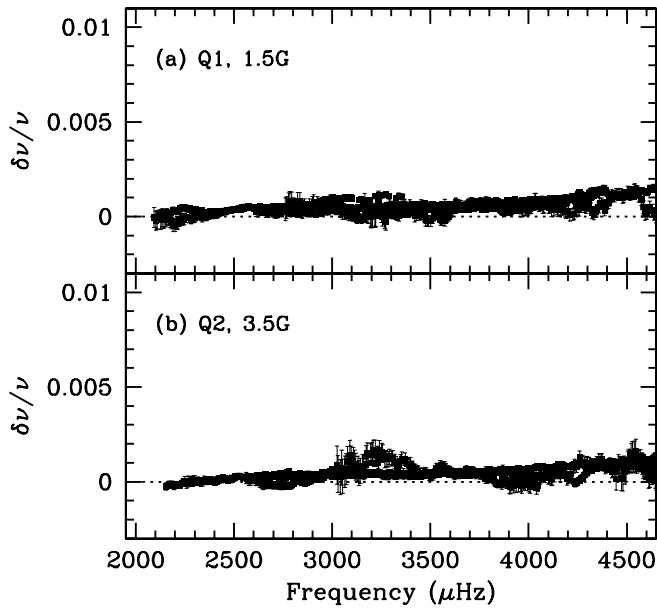


FIG. 2.—Relative frequency differences between the two pairs of quiet regions plotted as a function of frequency. The MAI difference between the two regions in each pair is noted in the figure.

$k^2 = l(l+1)/R_\odot^2$. Nevertheless, for the purpose of inversions we use “modes” with integral values of l so that the corresponding kernels from a standard solar model can be employed. Each data set gives about 1000 modes of oscillations in the range $2 \text{ mHz} \leq \nu \leq 4.5 \text{ mHz}$ and $0 \leq n \leq 6$, which are used for inversions. These are not strictly independent, as each mode is obtained by fitting a region of power spectrum that has significant overlap with those covered by neighboring modes.

For each of the regions listed in Table 1, we fit the power spectrum to get the frequencies of different modes as a function of (l, n) . Figure 2 shows the relative frequency differences between the two pairs of quiet regions used as control sets in this work. The difference between the MAI of the two regions in each pair is marked in the figure. The MAI differences are small, as are the frequency differences. Figure 3 shows the frequency differences between the different pairs of active and quiet regions used in this work. It can be seen that in general the frequency differences increase with increase in MAI, as has been seen in earlier work (Rajaguru et al. 2001). The frequency differences can become as large as 1%. For large MAI values ($\geq 100 \text{ G}$), the frequency differences become quite similar, and in some cases there is even a reduction in frequency differences as MAI increases. This saturation effect was also noticed by Rajaguru et al. (2001). The frequency differences increase with frequency and are only weakly dependent on n , except for NOAA 9906. It should be noted that these frequency differences are not scaled for mode inertia. If this scaling is applied, there will be significant dependence on n in the scaled frequency differences, as curves corresponding to different values of n will be scaled by different factors. The frequency differences between comparison spectra can be inverted to infer the differences in internal structure between the corresponding regions.

3. INVERSION TECHNIQUES

An inversion for solar structure (see, e.g., Dziembowski et al. 1990, 1994; Däppen et al. 1991; Antia & Basu 1994) generally proceeds through a linearization of the equations of stellar oscillations, using their variational formulation, around a known reference model. The differences between the structure

of the Sun and the reference model are then related to the differences in the frequencies of the Sun and the model by kernels. Nonadiabatic effects and other errors in modeling the surface layers give rise to frequency shifts (Cox & Kidman 1984; Balmforth 1992) that are not accounted for by the variational principle. In the absence of any reliable formulation, these effects have been taken into account in an ad hoc manner by including an arbitrary function of frequency in the variational formulation (Dziembowski et al. 1990).

The fractional change in the frequency of a mode can be expressed in terms of fractional changes in the structure of model characteristics, for example, the adiabatic sound speed c and density ρ and a surface term. The frequency differences can be written in the form

$$\frac{\delta\omega_i}{\omega_i} = \int_0^{1R_\odot} K_{c^2, \rho}^i(r) \frac{\delta c^2(r)}{c^2(r)} dr + \int_0^{1R_\odot} K_{\rho, c^2}^i(r) \frac{\delta \rho(r)}{\rho(r)} dr + \frac{F_{\text{surf}}(\omega_i)}{I_i} \quad (4)$$

(e.g., Dziembowski et al. 1990). Here $\delta\omega_i$ is the difference in the frequency ω_i of the i th mode between the data and the reference model, with i representing the pair (l, n) . The kernels $K_{c^2, \rho}^i$ and K_{ρ, c^2}^i are known functions of a reference solar model that relate the changes in frequency to the changes in c^2 and ρ , respectively. Instead of (c^2, ρ) , other pairs of functions can be used, such as density and adiabatic index Γ_1 . The integration is over distance r from the center of the Sun, extending to its surface radius $1 R_\odot$. The term in F_{surf} takes into account the near-surface errors in modeling the structure.

In this work, instead of inverting the differences between the frequencies of a model and those of the Sun, we invert the differences between the frequencies of active and quiet regions to determine the difference in structure between the two. Specifically, we determine the relative squared sound speed difference, $\delta c^2/c^2$, and the relative difference in the adiabatic index Γ_1 , $\delta\Gamma_1/\Gamma_1$. We still need to use a solar model to determine the kernels for the inversion. The use of the differences between two sets of solar frequencies instead of frequency differences between a model and the Sun ensures that we minimize any possible systematic error that may be caused by uncertainties in the solar model.

It should be noted that the expressions for the kernels were derived in the absence of magnetic field effects. In active regions the magnetic field will also cause frequency changes that must be included. In general, it may not be possible to distinguish between a thermal perturbation causing frequency shifts and a magnetic field causing similar shifts using only the mean frequencies, as we do in this work. Since we have not included possible contributions of the magnetic field, the inferred differences in sound speed may actually be due to the magnetic field. A change in sound speed can result indirectly from structural and thermal changes associated with the presence of magnetic fields, but the magnetic fields can also directly affect the sound speed by effectively modifying the wave propagation speed so that $\delta c^2/c^2 \sim v_A^2/c^2$, where v_A is the Alfvén speed. Furthermore, the inferred sound speed or magnetic field represents a horizontal average over the entire region studied in the ring-diagram technique. The active region itself may be much smaller. This is why the MAI values are much smaller than typical field strengths in sunspots.

Equations (4) constitute the inverse problem that must be solved to infer the differences in structure between the Sun and

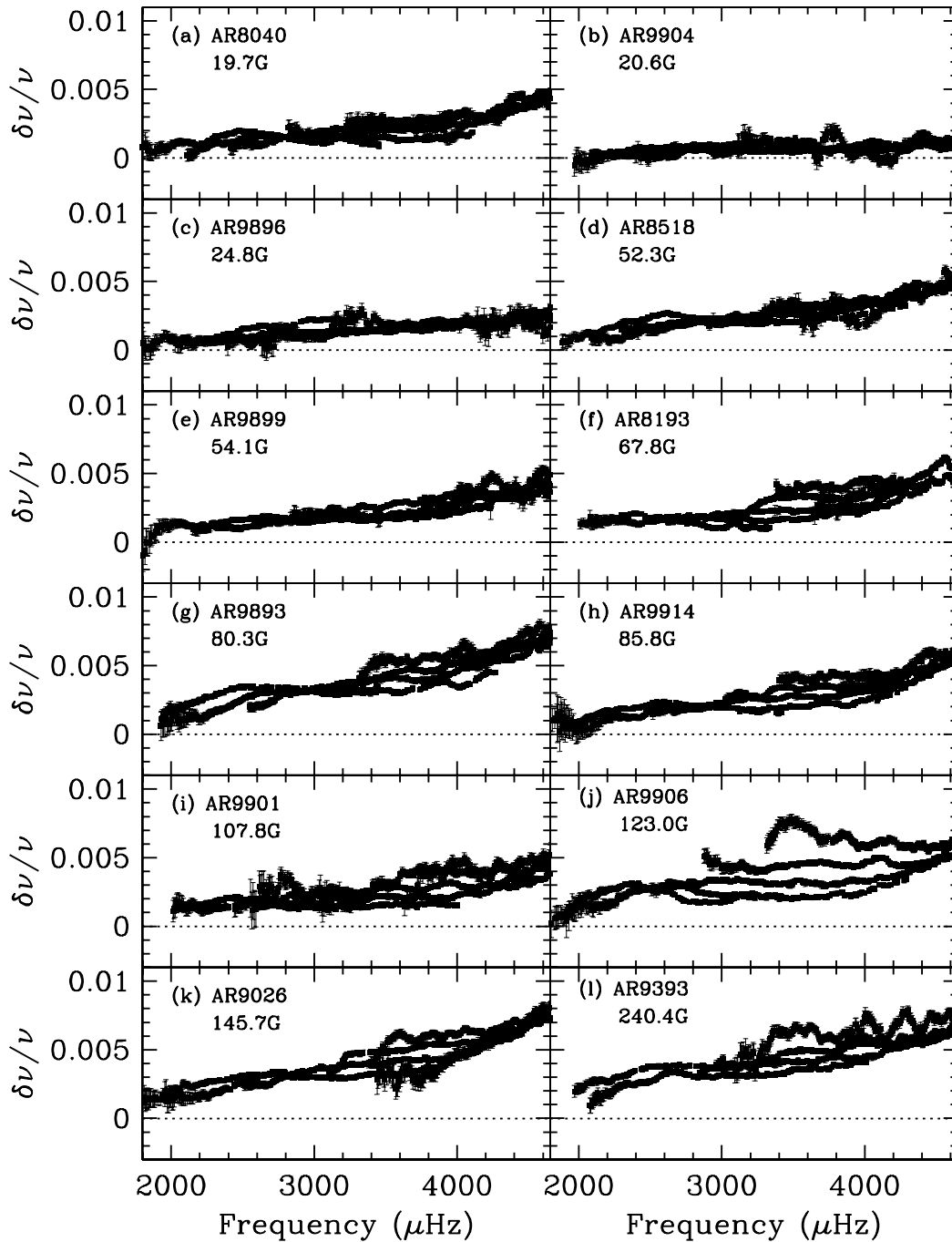


FIG. 3.—Relative frequency differences between the different pairs of active and quiet regions used in this work. Only the differences in the frequency range used in the inversions are shown. The field strength noted in each figure is the difference between the MAIs of the two regions in each pair, but since the MAIs of the quiet regions are always very small, less than 3 G, the differences are nearly equal to the MAIs of the active regions.

the reference model. They can be inverted using a variety of techniques. Most of the inversions in this work have been carried out using the subtractive optimally localized averages (SOLA) technique (Pijpers & Thompson 1992, 1994) or the regularized least squares (RLS) technique. Details of how SOLA inversions are carried out and how various parameters of the inversion are selected were given by Rabello-Soares et al. (1999). Details on RLS inversions and parameter selections were provided by Antia & Basu (1994) and Basu & Thompson (1996). Given the complementary nature of RLS and SOLA inversions (see Sekii 1997 for a discussion), if SOLA and RLS inversion results agree, we can be more confident of the results.

A set of averaging kernels obtained for sound-speed inversions using the SOLA technique is shown in Figure 4. The averaging kernels obtained for Γ_1 inversions are very similar. The averaging kernels show that we can get very good inversion results between about 0.975 and $0.998 R_\odot$ (i.e., between depths of about 1.4 and 18 Mm). The averaging kernels are well localized and have almost no side lobes. The width of the averaging kernels gives an indication of the resolution of the inversions. As can be seen, the resolution worsens with depth. This is not surprising, given that we do not have low- or intermediate-degree modes in the mode set. The averaging kernels become too wide to be useful below about $0.97 R_\odot$,

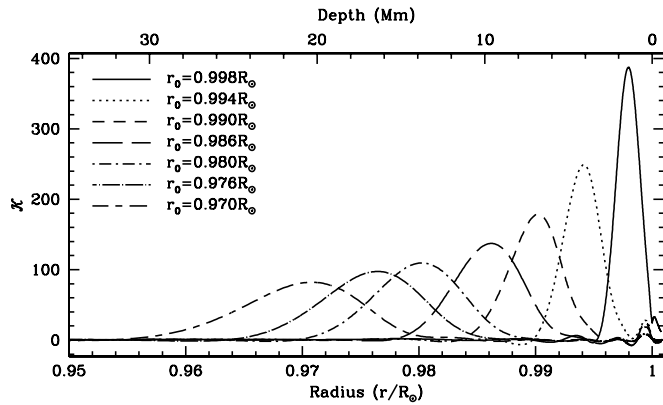


FIG. 4.—Sample of the averaging kernels obtained for determining the sound-speed differences between the active and quiet regions using the SOLA inversion technique. Each curve is labeled by the target radius for construction of the averaging kernel.

and we cannot construct any averaging kernel below about $0.96 R_{\odot}$.

4. RESULTS

The frequency differences between each pair of target regions were inverted to obtain the sound-speed differences. The sound-speed differences between the two pairs of control quiet regions are shown in Figure 5. Note that since we invert for the difference in the square of the sound speed, that is what is plotted in the figures (and $\delta c^2/c^2 = 2\delta c/c$). As can be seen from the figure, the SOLA and RLS inversions agree with each other within errors, and there is no significant difference in sound speed between the two pairs of quiet regions.

The sound-speed differences between the selected active regions and their comparison quiet regions are shown in Figure 6. The RLS and SOLA results agree well in almost all cases. As may be expected, the sound-speed differences are of the same order of magnitude as the frequency differences. In order to appreciate the role of the surface term in inversion results, we show in Figure 7 the residuals obtained in the RLS inversion for the region NOAA 9893. Figure 7a shows the observed scaled frequency differences. (The scaling factor Q_{nl} corrects for the fact that for the same perturbation, modes with smaller mode inertia are perturbed more than modes with larger mode inertia; see, e.g., Christensen-Dalsgaard & Berthomieu 1991.) There may be some uncertainty in estimating the mode inertia for high-degree modes because of uncertainties in modeling surface layers of the Sun. Major uncertainties in solar models are located at depths of less than about 1 Mm and should not unduly affect the modes that penetrate below that. This includes most of the modes used in the present study. It can be seen that modes of different n fall on different curves, indicating that the bulk of the frequency differences are due to structure variation in the interior and not to the surface term alone. Figure 7b shows what remains of the scaled frequency differences after removal of the surface term, while Figure 7c shows the residuals when only the structure contribution is removed. It can be seen that when the structure contribution is removed, the residuals are a function of frequency alone and can be attributed to the surface term. Furthermore, by comparing the different panels, we see that at low frequencies the surface term accounts for most of the observed frequency differences, while at high frequencies the structure contribution dominates. This frequency-dependent trend of the surface term is quite different

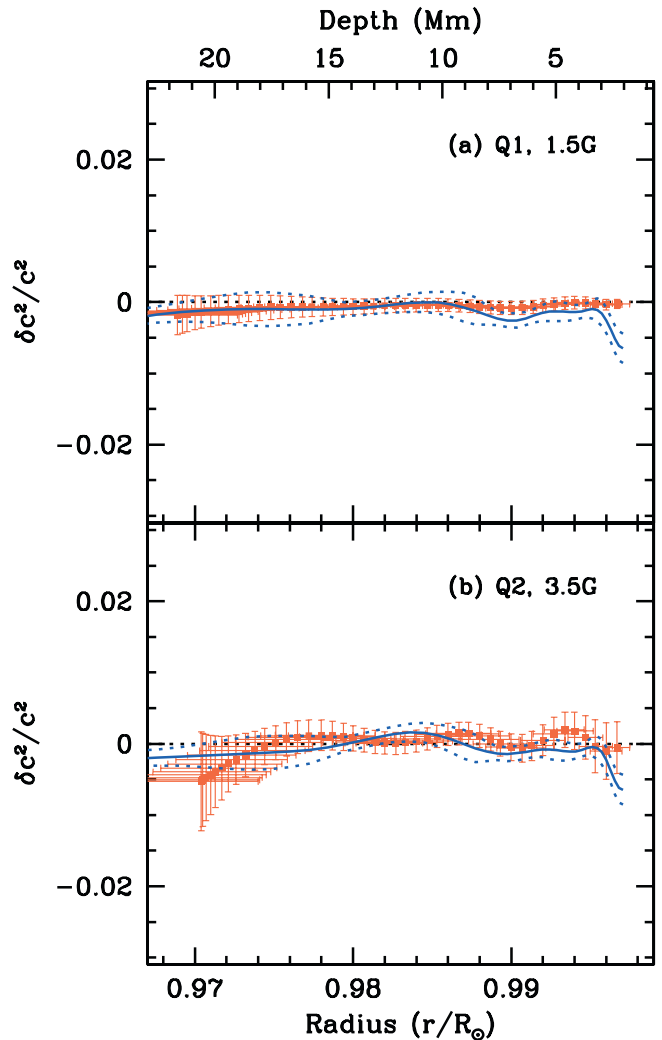


FIG. 5.—Relative differences of the squared sound speed between the two pairs of quiet regions obtained by inverting the frequency differences shown in Fig. 2. The blue solid line shows the RLS inversion results, with the blue dotted lines showing the 1σ error limit. The red points are the SOLA inversion results. The vertical error bars are the 1σ error, and the horizontal error bars mark the distance between the quartile points of the averaging kernels and are a measure of the resolution of the inversions.

from that in low-/intermediate-degree global modes where the surface term appears to dominate at higher frequencies. Figure 7d shows the residuals after removal of the contributions to the scaled frequency differences of both the structural terms and the surface term. These residuals are consistent with zero.

From Figure 6 we see that for active regions with low magnetic field (MAI values less than about 30 G), there is no significant difference in sound speed between the active and quiet regions. This is particularly true for NOAA 9904, which only emerged after the midpoint of the tracking interval. For active regions with stronger magnetic fields, we find a region just below the surface with negative sound-speed differences, i.e., a region where the sound speed below the active region is lower than that under the quiet region. At greater depths, the active regions have higher sound speed than the quiet regions. This is consistent with the inferences of Kosovichev et al. (2000, 2001) based on time-distance analysis. Kosovichev et al. (2000, 2001) find a decrease of about 10% in temperature (which can be interpreted as $\delta c^2/c^2 \approx 0.1$) at a depth of 4 Mm in a small active region (NOAA 8131) with an MAI of

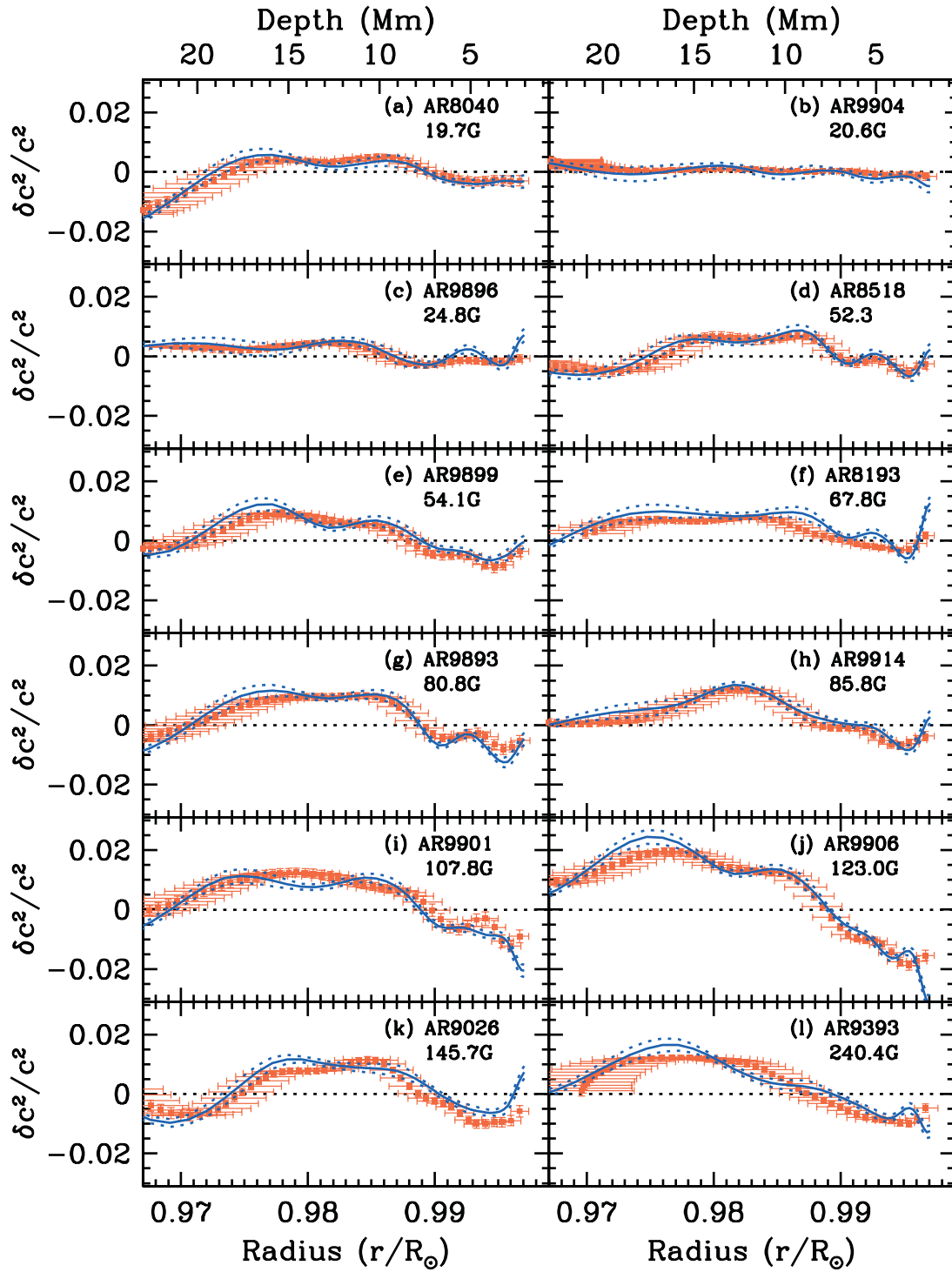


FIG. 6.—Relative differences of the squared sound speed between the different pairs of active and quiet regions obtained by inverting the frequency differences shown in Fig. 3. The blue solid line shows the RLS inversion results, with the blue dotted lines showing the 1σ error limit. The red points are the SOLA inversion results. The vertical error bars are the 1σ error, and the horizontal error bars mark the distance between the quartile points of the averaging kernels and are a measure of the resolution of the inversions.

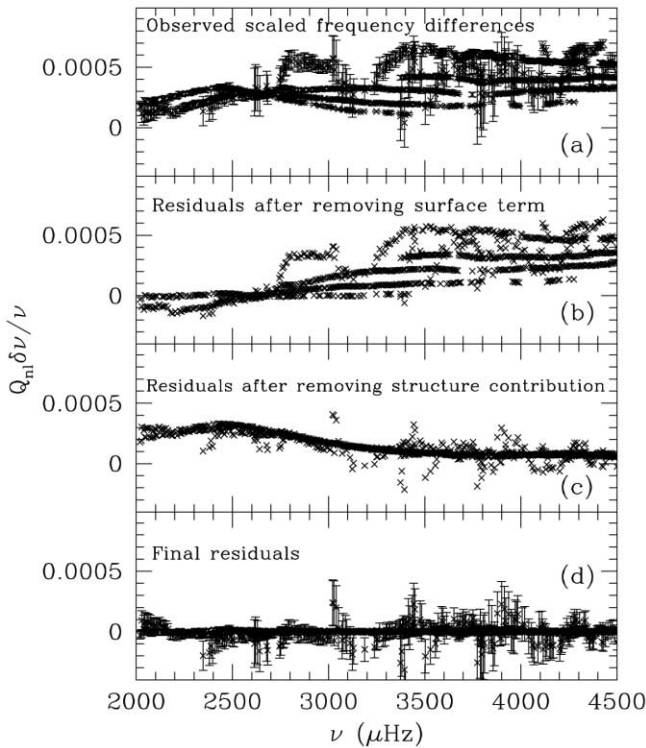


FIG. 7.—(a) Observed scaled frequency differences between the active region AR 9893 and the corresponding quiet region. (b) Scaled frequency differences that remain after removal of the surface term from the data in the top panel. (c) Surface term: the residuals obtained by removing the contribution due to differences in structure from the differences shown in the top most panel. (d) Residuals after the removal of the surface term and the contribution from the structural differences between the two regions. Error bars are shown only in two panels for the sake of clarity.

approximately 45 G and a maximum spot area of 340 millionths, or about 1.5% of our analysis region. Assuming that the full active region covers a few percent of our tracked region, this would imply a perturbation of about 0.005 in $\delta c^2/c^2$ over the tracked region in our analysis, which is consistent with the result we find for that depth and MAI.

The sound-speed differences between the active and quiet regions increase with increasing MAI of the active regions. In Figure 8 we show the average value of $\delta c^2/c^2$ in the radius ranges 0.978–0.984 R_\odot and 0.992–0.996 R_\odot . We see that the differences generally increase with MAI value, except at the highest value. In deeper layers the increase is roughly linear with MAI, while in the range 0.992–0.996 R_\odot the variation appears to be distinctly nonlinear. Similar behavior is seen in the frequency differences and the surface term, with the region of highest MAI value constituting a notable outlier to the general trend. The reason for this is not clear, but it can be noted that this region, NOAA 9393, produced a large number of flares during the observation period. It was also the largest active region considered in our study, extending over a large fraction of the 16° region analyzed, with a maximum spot area of about 13% of the total area. The original MDI Doppler measurements are very noisy in sunspots because of weakening of the line, poor signal-to-noise ratio, line asymmetries, and perhaps other effects. It is also possible that the occurrence of the flares affected the structure of the region; the oscillation frequencies are known to be affected by flares (Ambastha et al. 2003). There are also significant differences in the inversions using the two techniques in this case, possibly due to the noisier

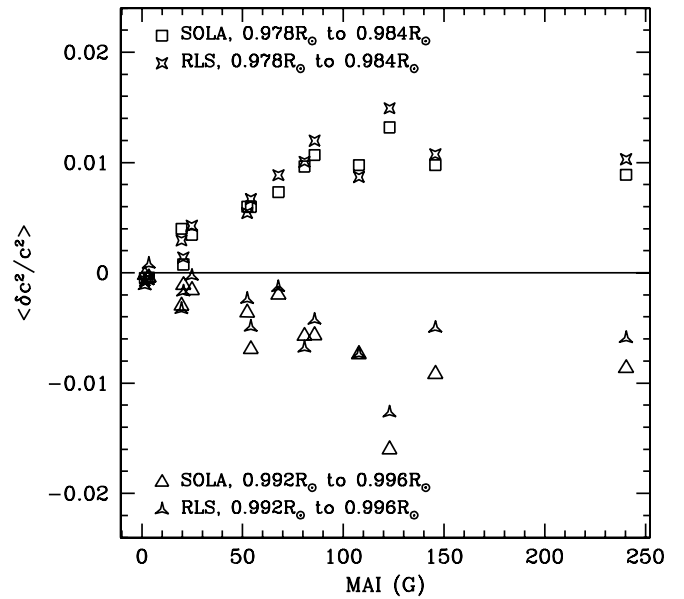


FIG. 8.—Mean squared sound-speed differences calculated between two depth ranges plotted against the magnetic activity index for the different active-quiet region pairs used in this work. Also plotted are the results for the two quiet-region pairs.

data, but also suggesting that the frequency changes may be more complex than what can be modeled by smooth variations in structure of the kind implicitly assumed in inversion techniques. The only other region that had extensive flare activity during the observations was NOAA 9026. This region had a much smaller area, however, as can be seen in Figure 1 and Table 1.

Although the sample of regions studied was too small to examine effects associated with the growth or decay of active regions, it is at least noteworthy that neither the most rapidly growing regions nor the most rapidly decaying ones appeared to differ in their structures from those of other more stable regions of comparable average strength.

In addition to modifying the structure, magnetic fields also have a direct effect on the frequencies of oscillations. To a first approximation, if we assume that $\delta c^2/c^2 \sim v_A^2/c^2$, we can estimate the magnetic field, even though the change in sound speed is likely to be a combined effect of the magnetic fields (via v_A) and the perturbation to the thermal structure caused by the magnetic field. Assuming an average $\delta c^2/c^2 \approx 0.01$ at a depth of 14 Mm below the surface, the inferred value for active regions with MAI ≈ 100 G, we get a magnetic field of the order of 40 kG at this depth, much larger than the measured surface values. This is not an unreasonable number: if the magnetic field does not increase significantly with depth, it will have negligible influence on the structure of these layers, and the observed differences will be concentrated near the surface. It should be noted that the inferred magnetic field is an average over the region studied; the sunspots themselves, which occupy only a small fraction of the area, have much stronger fields. Assuming that the sunspots occupy about 1/10 of the area covered by the observed region, the magnetic field in the spots should be about a factor of 3 higher than the inferred average value. At the solar surface, a magnetic field of 100 G will yield $v_A^2/c^2 \approx 0.006$. It is likely that this ratio remains of the same order up to a depth of 15 Mm, below which there may be some reduction in most cases.

Figure 9 shows the average surface terms for the different active regions plotted as a function of their MAI. The averages were taken between 2.2 and 2.6 mHz. As can be seen, the

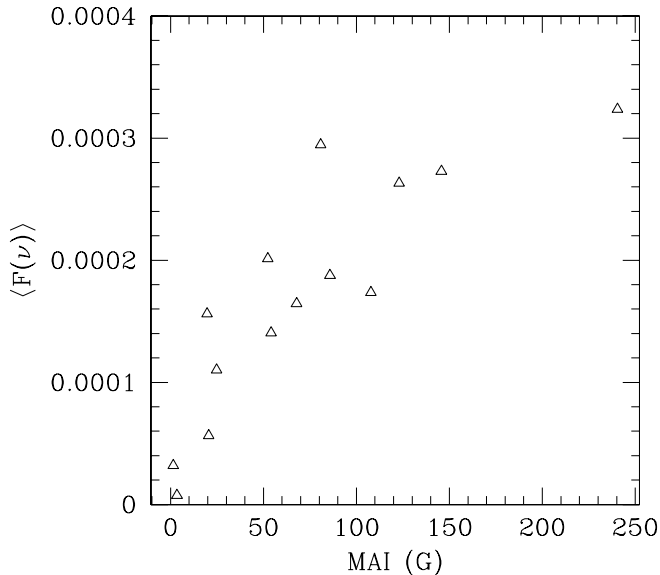


FIG. 9.—Surface term for the various pairs of regions, averaged over a frequency range of 2.2–2.6 mHz, plotted as a function of the MAI.

surface term increases with increase in MAI. This could possibly be an effect of the magnetic fields acting on and thereby modifying the boundary layers. The two flaring regions show a deviant trend compared with the other active regions: NOAA 9026 (147 G) has an unusually high surface term, while NOAA 9393 (242 G) has a surface term well below the trend.

In order to gain a better idea of what causes the sound-speed difference, we also invert to find the relative difference in Γ_1 between the active and quiet regions. The adiabatic index Γ_1 is determined by the equation of state and is expected to be close to 5/3 except in the ionization zones where it is reduced. Thus any difference in Γ_1 between an active and quiet region will be due to either a change in the effective equation of state associated with the contribution of the magnetic fields to the energy and pressure or to a shift in the depth of the ionization zones due to changes in the temperature profile below an active region, or a combination of both. Magnetic fields provide additional restoring forces and modify the frequency of modes. Since we have not explicitly accounted for the magnetic field, this effect manifests itself as a modification in the sound speed or Γ_1 . Within this framework the sound-speed differences are related to the Γ_1 difference by

$$\frac{\delta c^2}{c^2} = \frac{\delta \Gamma_1}{\Gamma_1} - \delta \ln \frac{P}{\rho}, \quad (5)$$

where P is the pressure and ρ is the density. Figure 10 shows the Γ_1 differences between the different pairs of active and quiet regions. As in the case of the sound-speed differences, we see that at low MAI there is no significant difference in Γ_1 between the regions. In other respects the Γ_1 differences look quite similar to the sound-speed differences shown in Figure 6. The subsurface negative difference peaks at a greater depth; otherwise the shapes are similar. As in the case of the sound-speed differences, the differences increase with increasing MAI.

It is relatively easy to change the speed of sound in a region, but changing Γ_1 is a more difficult proposition. The Γ_1 difference between active and quiet regions changes sign as we go from the near-surface regions inward. Although merely changing P , ρ , or T does not change Γ_1 , the change in the

ionization fractions associated with the thermal changes in the ionization zones does affect Γ_1 . It is difficult to explain a perturbation in Γ_1 of 2% in the He II ionization zone, however, as the entire variation in Γ_1 in this region is only of this order. It seems quite likely that the effect we are seeing is a combination of direct magnetic effects and related thermal effects, with direct effects probably dominating in deeper layers. Near the surface it is well known that the temperature in an active region is lower than that in a quiet region, and hence the differences may be dominated by thermal effect. However, in deeper layers the direct effects of magnetic fields may also contribute.

In order to further investigate the cause of the differences between the active and quiet regions, in Figure 11 we show the difference between the squared sound speed and Γ_1 perturbations. These can be interpreted as the relative differences in P/ρ , or equivalently in T/μ , where T is the temperature and μ is the mean molecular weight. From Figure 11 it can be seen that in the deeper layers, below about $0.98 R_\odot$, the sound-speed differences are explained by the Γ_1 differences and that within the error bars there is very little difference in P/ρ or T/μ . The situation is different at shallower depths, however. Above $0.98 R_\odot$, the difference shows a positive peak before becoming negative or near zero very close to the surface, at about $0.995 R_\odot$. Interpreting these differences as differences in either P/ρ or T/μ , we are led to the conclusion that at least around 0.98 – $0.99 R_\odot$, the magnetic fields of the active regions cause structural and associated thermal changes. In the deeper layers the mode frequency shifts may be due to the direct effects of the magnetic fields themselves.

5. CONCLUSIONS

In this work we have used the ring-diagram technique to study the difference in structure between active and quiet regions. The frequency difference between an active and a quiet region increases with the mean magnetic field strength in the active region, except at very high values of the MAI. The observed frequency difference can be inverted to obtain the corresponding difference in the structure of these regions. The sound speed in active regions is found to be lower in the layers just below the surface, while in deeper layers ($r < 0.99 R_\odot$) the sound speed is higher in the active regions. This is consistent with results obtained using the time-distance analysis (Kosovichev et al. 2000, 2001). The lower sound speed in the immediate subsurface layers could be a result of reduced temperature in active regions (Kosovichev et al. 2000). In all cases the differences in structure continue until a depth of at least 15 Mm. Below that, in most cases the perturbations tend toward zero. This presumably gives the extent to which the sunspots penetrate below the surface. However, since the resolution of inversion techniques deteriorates below a depth of 20 Mm, it is difficult to estimate this depth reliably. This estimate is consistent with the well-known observation that the solar rotation rate measured using sunspots is faster than the observed surface rotation rate and is close to the rotation rate of solar plasma at a depth of about 15–20 Mm as inferred using seismic techniques.

Looking at the magnitude of the inferred perturbations in the adiabatic index Γ_1 , it appears unlikely that they are due to either purely thermal or purely magnetic effects. They are most likely to be due to a combination of the direct effects of the magnetic field along with shifts in the ionization zones that result from temperature perturbations caused by these fields. We conclude that temperature perturbations seem to be the main cause of mode frequency shifts immediately below the surface, while magnetic fields are the likely cause of the variations in deeper layers.

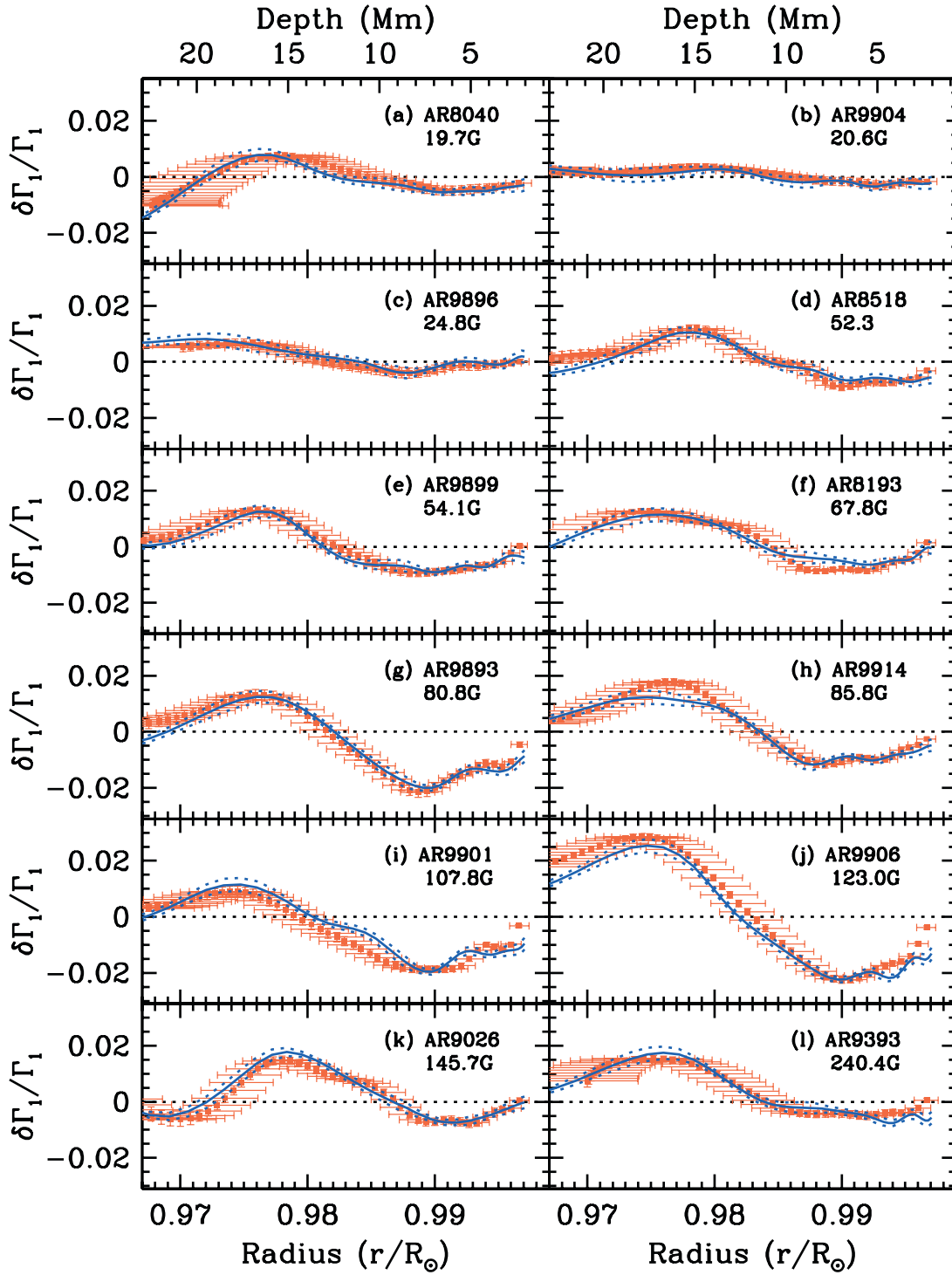


FIG. 10.—Relative differences of the adiabatic index Γ_1 between the different pairs of active and quiet regions obtained by inverting the frequency differences shown in Fig. 3. The different colors and line types are the same as in Figs. 5 and 6.

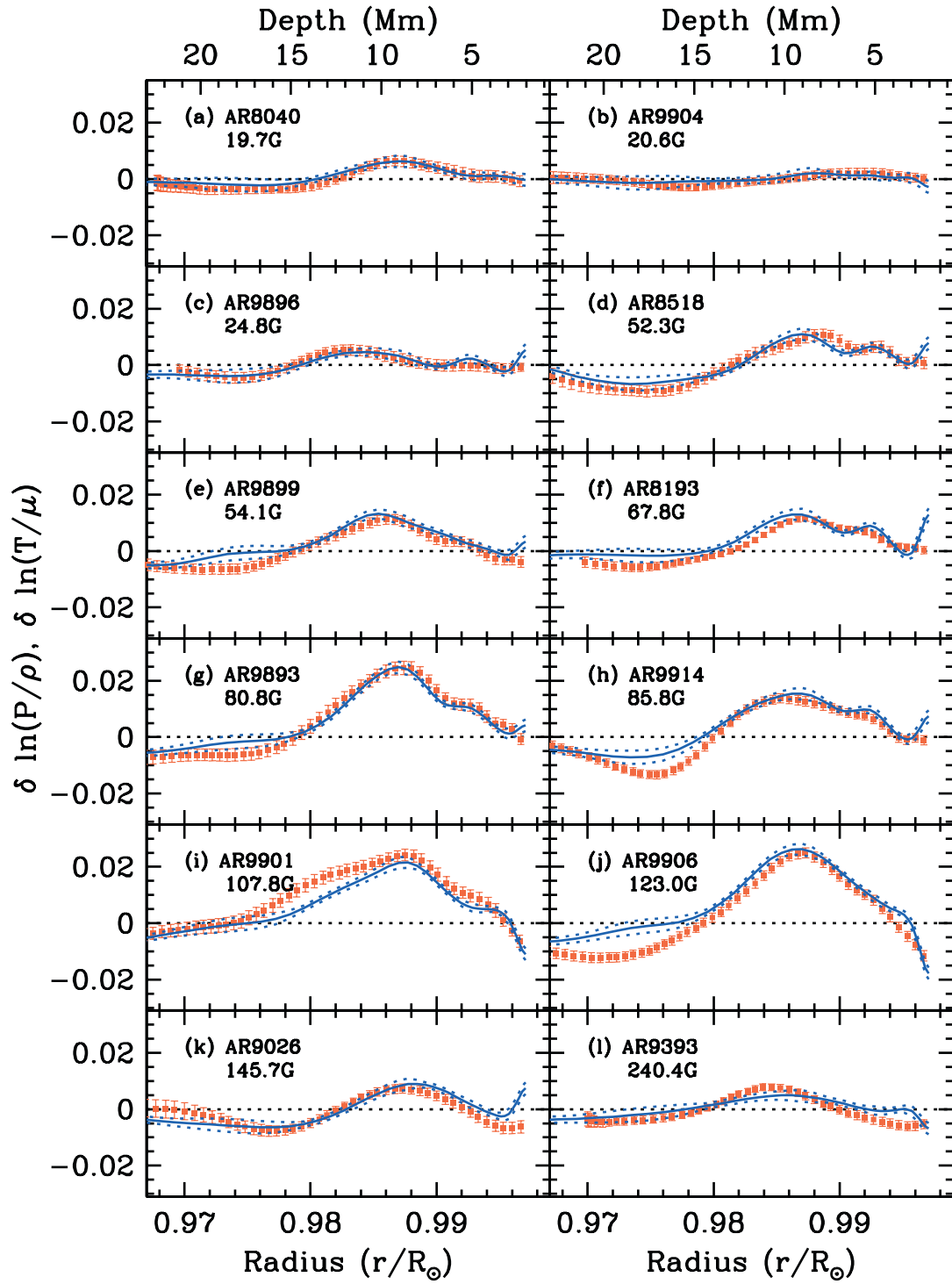


FIG. 11.—Difference between the $\delta c^2/c^2$ and $\delta \Gamma_1/\Gamma_1$ between the various pairs of active and quiet regions. These differences are equivalent to $\delta \ln(P/\rho)$ and $\delta \ln(T/\mu)$. The different colors and line types are the same as in Figs. 5 and 6.

This work utilizes data from the Solar Oscillations Investigation/Michelson Doppler Imager (SOI/MDI) on the *Solar and Heliospheric Observatory* (SOHO). The MDI project is supported

by NASA grant NAG5-8878 to Stanford University. *SOHO* is a project of international cooperation between ESA and NASA. This work was supported by NASA grant NAG5-10912 to S. B.

APPENDIX

DEFINING A LOCAL MAGNETIC ACTIVITY INDEX

Ring-diagram analysis is ordinarily carried out within arbitrarily defined compact circular or rectangular regions in a rotating surface coordinate system. True active regions are, of course, quite irregular in shape and time-varying as well. The present work is predicated on the assumption that it is at least possible to distinguish analysis regions of “high” magnetic activity from “normal” quiet regions, and that it is even possible to quantify (crudely) the level of magnetic activity with a single index parameter. For this purpose we have defined a *local* magnetic activity index (MAI) applicable to each analysis region during the time interval studied. This index was originally introduced in connection with a similar study by the present authors (Bogart et al. 2002) but has been used by others as well (e.g., Rajaguru et al. 2001), so a fuller explanation of the index is in order.

The regional MAI is formed by averaging the absolute values of the strong field ($|B_z| \geq 50$ G) pixels, after elimination of outliers, in the analysis region tracked from the MDI synoptic magnetograms over the analysis interval of 8192 minutes centered on the meridian crossing time of the target location. The magnetograms are made every 96 minutes, so these MAIs represent contributions from about 85 images. The individual averages of the filtered values from the appropriately remapped sector of each magnetogram are fitted to a linear trend in time; the MAI is the constant term in that two-parameter fit. The first-order term, a measure of the average rate of change of strong flux, is used to form a nondimensional growth rate parameter $GR = d \log(M)/d \log(t)$, where dM/dt is the first-order fit coefficient and M is the MAI. The characteristic time used is the tracking time, 8192 minutes.

The mapping that is used in forming the MAI is not actually Postel’s azimuthal equidistant projection used in the ring-diagram analysis, but rather Lambert’s azimuthal equal-area projection. This is to ensure that the average is a true average of flux, since the remapped pixels represent equal areas on the Sun. At the scale of the analysis regions, however, the differences between the two projections are negligible. The remapped values are subjected to the same spatial apodization used in preparing the Doppler power spectra, a roll-off of form $1 - x^4$ between radii of 15° and 16° , where x is the fractional distance into the apodization annulus.

The reason for restricting the contributing values to those in excess of 50 G is to avoid contamination by slight zero-level errors and residual noise in the measurements of the quiet-Sun values, which usually account for more than 99% of the pixels in a full-disk magnetogram and can severely bias the results even in a 15° window containing a large active region, let alone a comparison quiet region. It is a particular problem with the MDI magnetograms, because they are occasionally a mix of 5 minute and 1 minute averages, which have slightly different zero levels and noise levels. MDI 5 minute magnetograms typically have a central noise core with a FWHM of about 10 G (and 1 minute magnetograms about twice this, obviously), so the 50 G cutoff ensures that the number of contributing “noise” pixels is small compared with the number of “signal” pixels even in generally quiet areas.

Outliers are defined as pixels with field values differing by a factor of more than 6 from the average of their neighbors, if that average is more than 400 G. These are generally due to cosmic-ray hits to the detector and are quite infrequent, typically about 0.5 pixel per full-disk magnetogram, and seldom more than 5.

REFERENCES

- Ambastha, A., Basu, S., & Antia, H. M. 2003, *Sol. Phys.*, 218, 151
 Anderson, E. R., Duvall, T. L., Jr., & Jefferies, S. M. 1990, *ApJ*, 364, 699
 Antia, H. M., & Basu, S. 1994, *A&AS*, 107, 421
 Antia, H. M., Basu, S., Hill, F., Howe, R., Komm, R. W., & Schou, J. 2001, *MNRAS*, 327, 1029
 Balmforth, N. J. 1992, *MNRAS*, 255, 632
 Basu, S., & Antia, H. M. 1999, *ApJ*, 525, 517
 Basu, S., Antia, H. M., & Tripathy, S. C. 1999, *ApJ*, 512, 458
 Basu, S., & Thompson, M. J. 1996, *A&A*, 305, 631
 Birch, A. C., Kosovichev, A. G., Price, G. H., & Schlottmann, R. B. 2001, *ApJ*, 561, L229
 Bogart, R. S., Basu, S., & Antia, H. M. 2002, in *Proc. SOHO 11 Symp., From Solar Min to Max: Half a Solar Cycle with SOHO*, ed. A. Wilson (ESA SP-508; Noordwijk: ESA), 145
 Christensen-Dalsgaard, J., & Berthomieu, G. 1991, in *Solar Interior and Atmosphere*, ed. A. N. Cox, W. C. Livingston, & M. S. Matthews (Tucson: Univ. Arizona Press), 401
 Cox, A. N., & Kidman, R. B. 1984, in *Proc. 25th Liège Int. Astrophys. Colloq., Theoretical Problems in Stellar Stability and Oscillations* (Liège: Univ. Liège, Institut d’Astrophysique), 259
 Däppen, W., Gough, D. O., Kosovichev, A. G., & Thompson, M. J. 1991, in *Challenges to Theories of the Structure of Moderate-Mass Stars*, ed. D. O. Gough & J. Toomre (Berlin: Springer), 111
 Duvall, T. L., Jr., Jefferies, S. M., Harvey, J. W., & Pomerantz, M. A. 1993, *Nature*, 362, 430
 Dziembowski, W. A., Goode, P. R., Pamyatnykh, A. A., & Sienkiewicz, R. 1994, *ApJ*, 432, 417
 Dziembowski, W. A., Pamyatnykh, A. A., & Sienkiewicz, R. 1990, *MNRAS*, 244, 542
 Gizon, L., & Birch, A. C. 2002, *ApJ*, 571, 966
 Gough, D. O., et al. 1996, *Science*, 272, 1296
 Hill, F. 1988, *ApJ*, 333, 996
 Hindman, B., Haber, D., Toomre, J., & Bogart, R. 2000, *Sol. Phys.*, 192, 363
 Jensen, J. M., Duvall, T. L., Jr., & Jacobsen, B. H. 2003, in *Proc. SOHO 12/GONG+ 2002 Workshop, Local and Global Helioseismology: The Present and Future*, ed. H. Sawaya-Lacoste (ESA SP-517; Noordwijk: ESA), 315
 Korzennik, S. G. 2001, in *Proc. SOHO 10/GONG 2000 Workshop, Helio- and Asteroseismology at the Dawn of the Millennium*, ed. A. Wilson (ESA SP-464; Noordwijk: ESA), 149
 Kosovichev, A. G., Duvall, T. L., Jr., Birch, A. C., Gizon, L., Scherrer, P. H., & Zhao, J. 2001, in *Proc. SOHO 10/GONG 2000 Workshop, Helio- and Asteroseismology at the Dawn of the Millennium*, ed. A. Wilson (ESA SP-464; Noordwijk: ESA), 701
 Kosovichev, A. G., Duvall, T. L., Jr., & Scherrer, P. H. 2000, *Sol. Phys.*, 192, 159
 Nigam, R., & Kosovichev, A. G. 1998, *ApJ*, 505, L51
 Patrón, J., et al. 1997, *ApJ*, 485, 869
 Pijpers, F. P., & Thompson, M. J. 1992, *A&A*, 262, L33
 ———. 1994, *A&A*, 281, 231
 Rabello-Soares, M. C., Basu, S., & Christensen-Dalsgaard, J. 1999, *MNRAS*, 309, 35
 Rajaguru, S. P., Basu, S., & Antia, H. M. 2001, *ApJ*, 563, 410
 Sekii, T. 1997, in *IAU Symp. 181, Sounding Solar and Stellar Interiors*, ed. J. Provost & F.-X. Schmider (Dordrecht: Kluwer), 189